The Astrophysical Journal, 996:56 (9pp), 2026 January 1 https://doi.org/10.3847/1538-4357/ae22d5

A Jovian Decametric Emission Event Observed Locally by Juno and Remotely by Wind and STEREO-A at 1 au

Ruobing Zheng[1,2], Yuming Wang[1,2,3], and Chuanbing Wang[1,2]
[1] National Key Laboratory of Deep Space Exploration/School of Earth and Space Sciences, University of Science and Technology of China, Hefei 230026, People's Republic of China; ymwang@ustc.edu.cn
[2] CAS Center for Excellence in Comparative Planetology/CAS Key Laboratory of Geospace Environment, University of Science and Technology of China, Hefei 230026, People's Republic of China
[3] Hefei National Laboratory, University of Science and Technology of China, Hefei 230088, People's Republic of China
Received 2025 July 23; revised 2025 November 17; accepted 2025 November 19; published 2025 December 24

Abstract

Juno in situ observations provide insightful data on plasma, electric, and magnetic fields associated with Jovian decametric (DAM) emission, while remote-sensing observations offer broader spatial and temporal coverage. Combining both perspectives may help us understand the dynamic processes of DAM radiation. In this work, we present an Io-related DAM emission continued intermittently for at least 2 hr, observed by Juno in situ and remotely by Wind and STEREO-A. The Io-DAM emission evolved from three discrete narrow arcs to one mixed broad arc within 11 minutes in remote-sensing dynamic spectra. The source remained near a lead angle of 6° from the main Alfvén wing spot during the observation. Juno/JADE detected peaks in electron energy flux and an upward loss-cone distribution. Using a set of resonance circles, we estimate a maximum growth rate γ/ω_c of 6.4×10^{-4}, corresponding to electron energies of 0.2–10 keV and emission angles of 77°–88°. Meanwhile, we infer the properties of the source region of the event from the remote-sensing observations at 1 au. The inferred results on electron energy, emission angle, and source locations are consistent with the Juno in situ observations, suggesting the consistent properties of this Io-DAM event over 2 hr observational intervals. This consistency also reinforces the reliability of the remote sensing inversion method. Our work contributes to the establishment of long-term stereoscopic remote monitoring, addressing limitations in local observational coverage and enhancing our understanding of the dynamic processes of DAM emission.

Unified Astronomy Thesaurus concepts: Solar system astronomy (1529); Planetary science (1255); Planetary magnetospheres (997); Magnetospheric radio emissions (998); Remote sensing (2191); Radio observatories (1350); Jupiter (873); Jovian satellites (872)

1. Introduction

The exploration of Jupiter's magnetosphere and its dynamic interactions has been significantly augmented with the arrival of the Juno spacecraft in 2016 July. Juno's unique polar orbit, regularly traversing Jupiter's auroral regions, has provided unprecedented opportunities for in situ measurements of the planet's auroral emissions and plasma environment (F. Bagenal et al. 2017). Juno's instrumentation suite, including JADE, Waves, and magnetometer (MAG), has enabled detailed observations of Jupiter's auroral regions, offering insights into the generation mechanisms of intense Jovian radio emissions (J. E. P. Connerney et al. 2017; W. S. Kurth et al. 2017; D. J. McComas et al. 2017). P. Louarn et al. (2018) suggested that electron conic distributions, which provide free energy and play a crucial role in wave generation through the cyclotron maser instability (CMI) theory (C. S. Wu & L. C. Lee 1979; D. Le Quéau et al. 1984a, 1984b; C. S. Wu 1985; P. L. Pritchett 1986), are commonly observed in Jovian radio sources. C. K. Louis et al. (2019b) revealed that the sources of Jovian auroral radiation at kilometer and decameter wavelengths are magnetically connected to regions of far-ultraviolet (FUV) emissions based on Juno's first 15 perijoves. Furthermore, C. K. Louis et al. (2020) detected radio emissions during the crossing of magnetic field lines connected to Ganymede's tail, with simultaneous FUV observations by J. R. Szalay et al. (2020).

On the other hand, remote-sensing observations offer a broader perspective, covering large spatial and temporal scales, and thus complement the localized measurements provided by Juno. Various ground-based radio telescopes have been employed for long-term monitoring of Jovian decametric (DAM) emissions, including the Nançay Decameter Array (A. Lecacheux 2000), the Ukrainian UTR-2 array (A. Konovalenko et al. 2016), and NenuFAR (P. Zarka et al. 2015). In addition, radio dynamic spectra from spacecraft such as Wind (J. L. Bougeret et al. 1995), STEREO (J. L. Bougeret et al. 2008), Cassini (D. A. Gurnett et al. 2004), and Juno provide multiangle views of Jupiter's radio emissions, helping to characterize their properties and identify the associated source regions.

Based on the loss-cone-driven CMI theory, S. Hess et al. (2008, 2010) established an emission angle function dependent on active electron energy and the Jovian magnetic field. This function has become fundamental to several remote-sensing methods to infer the source locations and emission properties of DAM emissions, including the ExPRES code (C. K. Louis et al. 2019a), the updated lead angle model (L. Lamy et al. 2022), and the method developed by Y. Wang et al. (2020, 2022). Specifically, S. Hess et al. (2010) fitted the Io-DAM arcs and summarized an empirical relationship between resonant electron energy and Io's position in System III (SIII)

longitude. Using the updated lead angle model, L. Lamy et al. (2022) traced Io-DAM source locations and fitted 11 Io-DAM arcs with an energy of 3–16 keV. Meanwhile, Y. Wang et al. (2020, 2022) used the empirical emission characteristics (energy and beaming angle) to constrain and trace all the potential DAM sources independent of the Io-DAM lead angle. Adopting Wang's approach, R. Zheng et al. (2023) statistically analyzed 81 Io-DAM and non-Io-DAM (auroral DAM) emissions from multiview observations, identifying resonant electron energies between 2 and 22 keV. Remote-sensing inversion methods effectively trace potential DAM source regions and estimate emission characteristics—such as resonant electron energy and beaming angle—as they evolve over observational timescales. These methods are particularly valuable for analyzing emission dynamics over periods of hours. Nevertheless, inversion results derived from remote-sensing techniques inherently carry greater ambiguity compared to direct in situ measurements.

By integrating in situ and remote-sensing observations, we may not only verify the methods used to infer the DAM properties from remote-sensing data that facilitate the establishment of long-term observations for statistical properties but also gain a deeper understanding of the complex processes driving Jupiter's decametric radio emissions. In this study, we survey Juno's in situ data to identify radio source crossings (Section 2.1) and employ the inversion method developed by Y. Wang et al. (2020) based on remote-sensing observations from Wind and STEREO (Section 2.2). By combining these observations and methods, we analyze a clear Io-DAM event jointly observed by Juno locally and Wind and STEREO-A (STA) remotely (Sections 3 and 4). Section 4 summarizes and discusses the results.

2. Observation and Method

2.1. Juno In Situ Observation and Identification of DAM Crossings

The Juno mission (F. Bagenal et al. 2017) with its polar orbit covers a broad radial range and repeatedly threads auroral field lines at a range of very low altitudes that are almost certainly sampling the auroral acceleration region and the sources of auroral radio emissions. Equipped with the Waves instrument (W. S. Kurth et al. 2017), Juno carries a 4.8 m dipole electric antenna connected to two receivers, capturing the entire frequency range of Jovian radio auroral emissions. The low-frequency receiver samples the frequency bands of 50 Hz–20 kHz and 10–150 kHz, intended for plasma and radio wave analysis, whereas the high-frequency receiver (HFR) covers 150 kHz–3 MHz and 3–41 MHz bands. Additionally, Juno/Waves can operate in a burst-mode waveform, sweeping a 1 MHz bandwidth including the local electron cyclotron frequency (f_{ce}) every second during perijoves, achieving the resolution required to identify DAM crossings in the spectrum. We adopt the same identification criterion as P. Louarn et al. (2018): radiation signals detected at frequencies within 1–1.01 f_{ce}, following the observations by P. Louarn et al. (2017), who identified CMI-driven radio emissions occurring at frequencies slightly exceeding f_{ce} by about 1%.

2.2. Remote-sensing Observations and Inversion Method

The Wind and STEREO missions provide a near-Earth stereoscopic view of Jovian radio emissions at 1 au. The Wind spacecraft is located around the first Lagrange point of the Sun–Earth system. It carries the WAVES instrument (J. L. Bougeret et al. 1995) to provide measurement of radio and plasma waves. We use the radio receiver band 2 to get electric field data in a frequency range of 1.075–13.825 MHz with a 50 kHz frequency step. The STEREO mission consists of twin spacecraft that were ahead of STA and behind STEREO-B (STB) the Earth at launch, orbiting the Sun at nearly 1 au. We choose the STA spacecraft due to the lost communication of STB before the Juno mission. Similarly, the STEREO/WAVES instrument (J. L. Bougeret et al. 2008) includes an HFR, operating in the 0.125–16.075 MHz range.

For remote-sensing observations, the available data are the dynamic spectra of radio waves, and an inversion method is required to analyze the source region and radiation properties of radio emissions. We use the inversion method developed by Y. Wang et al. (2020) and statistically applied by R. Zheng et al. (2023). This method utilizes the characteristics of observed DAM arcs to determine the quadrant of Jupiter and search for active magnetic field lines originating from that quadrant. These active field lines are searched by matching the following function with the time–frequency drift pattern observed in DAM arcs. The function is provided by S. Hess et al. (2008):

$$\theta_b = \arccos\left(\frac{v}{Nc}\cdot\frac{1}{\sqrt{1-\frac{\omega}{\omega_{ce,max}}}}\right), \quad (1)$$

in which θ_b is the beam angle, v the electron velocity, c the light speed, N the refraction index, w the observed frequency of the radio emission, and $w_{ce,max}$ is the maximal electron cyclotron frequency at the active field line footprint. We set $w_{ce,max}$ to be the value at 900 km altitude, as it corresponds to the typical altitude of the Io ultraviolet (UV) footprint (B. Bonfond et al. 2009). It is important to note that Equation (1) is based on electron loss-cone-driven CMI, which has been observed in the Jovian magnetosphere through Juno in situ observations (e.g., P. Louarn et al. 2017, 2018; C. K. Louis et al. 2020). This function presupposes that the CMI resonance circle leading to maximum amplification is tangent to the border of the loss cone with pitch angle α, where the resonance circle center $v_{\|0}$ locates at $v/\cos\alpha$. On the other hand, according to the CMI resonance condition in the weakly relativistic case, the resonance circle center is given as $v_{\|0} = k_{\|}c^2/w_{ce} = (w/w_{ce})cN\cos\theta_b$. Thus, the emission angle can be expressed by Equation (1). When searching for active field lines, certain constraints are applied based on previous studies: (1) the cone wall thickness is less than 2°, (2) the emission angle ranges from 55° to 90°, and (3) the electron energy is above 0.2 keV (detailed in Y. Wang et al. 2022). Jupiter's magnetic field is modeled by combining the internal magnetic field based on the *JRM33* model (J. E. P. Connerney et al. 2022) with an extended field based on the current sheet model *CAN20* (J. E. P. Connerney et al. 2020).

3. The 2017 March 27 Event

We used data from the MAG and Waves instruments from Juno 1 to 36 perijoves (PJ, and PJ 2 lacks data) to identify DAM source crossings based on the criteria in Section 2.1 and found a total of 59 source crossings, of which 48 crossings are from the

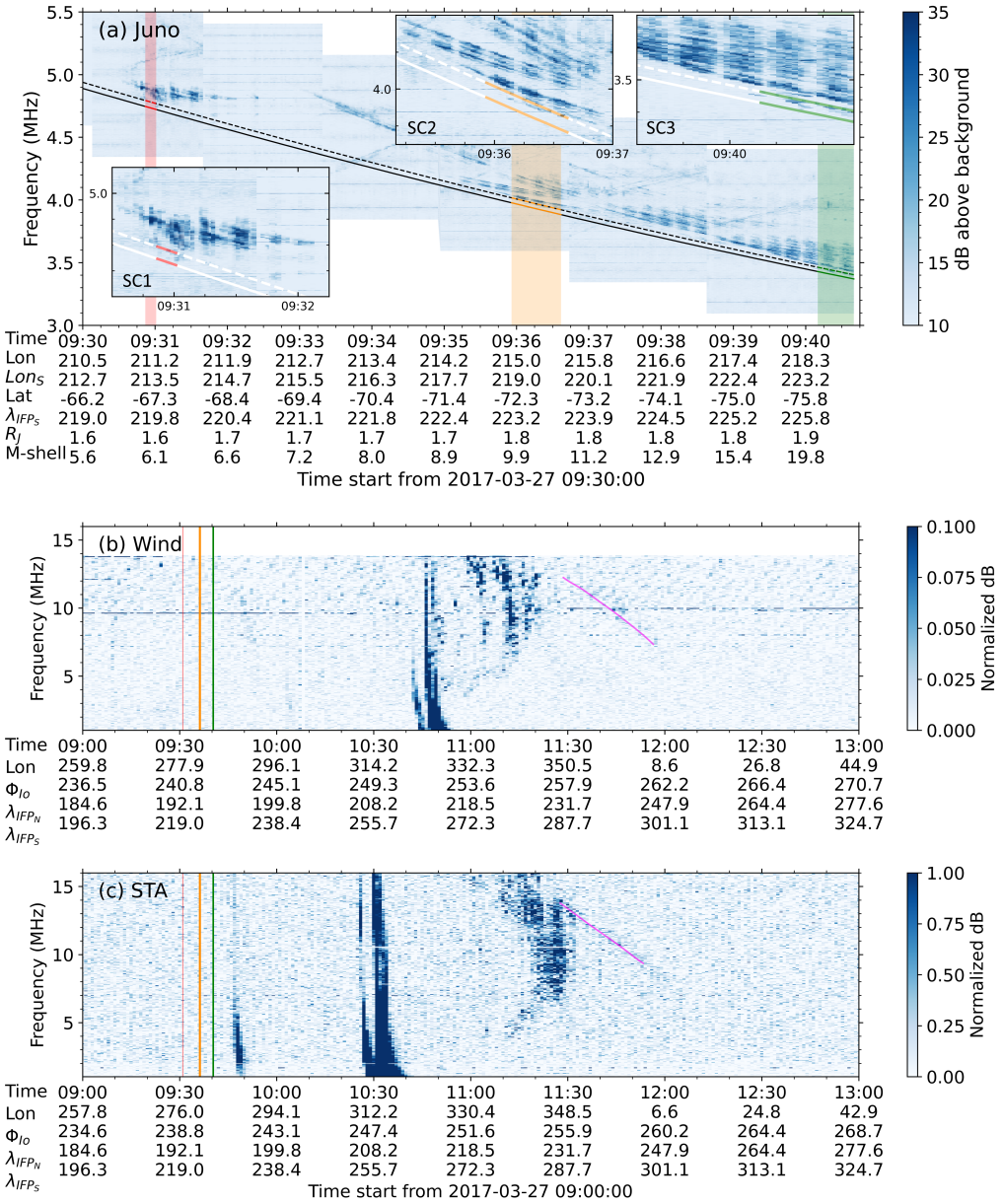

Figure 1. The multiview dynamic spectra for the DAM event on 2017 March 27. Panel (a) shows Juno/Waves dynamic spectra from 3 to 5.5 MHz with three DAM source crossings (red, orange, and green segments). Local zoom-in views of the three source regions (SC1, SC2, and SC3) are also shown. The solid and dashed lines indicate the local electron cyclotron frequency f_{ce} and 1.01 f_{ce}. Panels (b) and (c) show the remote-sensing spectra observed by Wind and STA from 2 to 16 MHz (excluding light travel time from the Jovian surface to the spacecraft, hereafter), with the vertical lines corresponding to the time range in panel (a). The purple lines indicate two weak emission features that may correspond to a non-Io-C emission. In the legend, *Lon* and *Lat* represent the spacecraft's position in the west SIII coordinate; Φ_{Io} is the phase of Io; $\lambda_{IFP_{N,S}}$ is the north (or south) hemisphere footprint of Io in longitude; and Lon_S is the Juno's projected longitude in the southern hemisphere, which is calculated based on the magnetic field model *JRM33+CAN20* (J. E. P. Connerney et al. 2020, 2022).

northern hemisphere and 11 from the southern hemisphere. Then, we searched if the DAM arc appears in the spectra of Wind and STA within a 10 hr time window centering at a given source crossing of Juno. We analyzed the geometry of the three spacecraft, the characteristics of the DAM arc, and source crossing in the spectra (detailed below) to determine whether it is the same event. Finally, we obtained only one definite case that is consistent with the multipoint observations.

3.1. The Overall Picture

Multiview dynamic spectra of the DAM event are illustrated in Figure 1. Based on the selection criteria, three DAM source crossings (SC1–3) are identified in panel (a) from Juno observations at 09:30:52–09:31:01, 09:35:56–09:36:37, and 09:40:10–09:40:40, respectively. Here and hereafter, we use the local time at Jupiter if not specifically noted. For Wind and STA, timestamps are corrected by subtracting the light travel time from Jupiter to each spacecraft. The position of Juno indicates that the source regions of all three episodes are located in the southern hemisphere, with corresponding SIII longitudes (Lon or Central Meridian Longitude, CML) of 213°–223°, close to the projected location of Io and its wake. In addition, the M-shell value of 6 for the first crossing is near that of Io's orbit ($M \sim 5.9$), and the latter two source regions

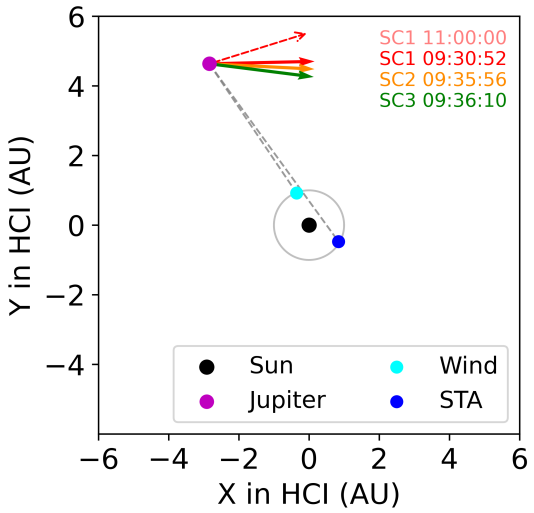

Figure 2. Geometric configuration of Jupiter, Wind, and STA in the HCI coordinate system, with colored arrows showing antiparallel magnetic field directions at DAM source regions: solid arrows for in situ Juno crossings (SC1-SC3), and a red dashed arrow for SC1's projected Io footprint after corotation at 11:00 UT.

have M-shell values of 10 and 20, which lie in the typical range of active non-Io-DAM source regions ($M = 7$–60), as reported by C. K. Louis et al. (2019b). Hence, it is probable that Juno has crossed an Io-DAM emission first, followed by the next two traversals of the non-Io-DAM source regions.

Approximately 1.5 hr later, a DAM emission cone swept through the directions of the Wind and STA, sequentially, as shown in panels (b) and (c) of Figure 1. These DAM arcs resemble closed parentheses and correspond to the CML of 330°–350° and an Io phase of 250°–260°. Around the vertex frequency, Wind observes emissions from 11:02 to 11:17 and STA from 11:11 to 11:28. Since the angular separation of the Wind and STA was 2° with respect to Jupiter and the time interval for the DAM arcs swept from Wind to STA was ∼11 minutes, we may estimate that the apparent angular velocity of the DAM emission cone was about 0.3 Ω_j (Ω_j is Jupiter's rotational angular velocity), close to Io's rotational angular velocity around Jupiter (i.e., 0.23 Ω_j). Thus, it is an Io-related emission for the DAM arcs. Based on previous empirical analysis of the CML-Io phase diagram (M. S. Marques et al. 2017), this Io-DAM emission can be classified as an Io-C event, located in the southeastern hemisphere of the near-Earth view.

The above analysis suggests that the arcs observed by the Wind and STA probably originated from the same source region of the first DAM crossing by Juno. The DAM event continued intermittently for at least 2 hr from about 09:30 to 11:30. As revealed by the Wind and STA radio dynamic spectra, the emission evolved from three discrete narrow arcs to one mixed broad arc within 11 minutes. It should be noted that the other two non-Io-DAM source crossings of Juno do not have a clear imprint in the Wind or STA radio dynamic spectra. A weak candidate can be found between 11:30 and 12:00, as indicated by the purple lines. The time difference between the two features suggests a rotational angular velocity of 1.2 Ω_j, which may correspond to the non-Io-C emission.

Figure 2 illustrates the geometric configuration of Jupiter, Wind, STA, and the active magnetic field lines associated with the DAM source regions in the Heliocentric Inertial (HCI) coordinate system. At approximately 09:30 UT, the magnetic field directions of the three source crossings by Juno in situ (colored solid arrows) formed separation angles of about 45°–60° with respect to the Jupiter-Wind and Jupiter-STA lines of sight. As the source corotated with Jupiter's magnetic field, the separation angle of SC1 gradually increased and approached 90° by 11:00 UT (red dashed arrow), indicating that the DAM emission could be directed toward near-Earth spacecraft, thus becoming more favorable for its detection by Wind and STA.

3.2. The Electron Energy and Emission Angle

As shown in Figure 3(a), the electron energy flux from Juno/JADE shows a significant enhancement during the three source crossings in Figure 1. The first source crossing with the brief time indicates the small spatial scale of the active field line for the Io-DAM emission. The interval of 09:37–09:39 between the second and third crossings also shows high energy flux, probably because Juno was close to the non-Io-DAM source region. For active electrons at 2–22 keV in Figure 3(b), we can find that the number density in the phase space was clearly reduced within the pitch angle of 160°–180° (in the south hemisphere) compared to the opposite direction during the second and third crossings. It means that a loss cone existed at that pitch angle. During the first crossing, pitch-angle data below 45° are unavailable, and for the upward-going electrons (above 90°), the phase-space density (PSD) decreases toward 180°.

Figures 4((a)–(c)) show three snapshots of density distribution in the phase space. The snapshot of SC1 at 09:30:53 in panel (a) shows that a loss cone appears in the upward direction with a pitch angle of 155°–180°. The snapshot of SC2 at 09:36:01 in panel (b) displays a sharp loss cone at 165°–180°. Panel (c) for SC3 at 09:40:19 maintains similar loss-cone characteristics as SC2 and has a decrease in overall PSD. To obtain more accurate results, we first use the cubic interpolated data to calculate the gradient of the distribution and integration (detailed in the Appendix) and then apply the following technique to find the resonance circle where the largest growth rate appears.

The CMI theory is widely applied in planetary radio emission and detailed in D. Le Quéau et al. (1984a, 1984b), P. L. Pritchett (1986), C. S. Wu (1985), and C. S. Wu & L. C. Lee (1979). For a DAM source, X-mode waves ($\omega/k_\parallel c \gg 1$) dominate, propagating close to the electron gyrofrequency ($\omega \sim \omega_c$) in a low-density ($\varepsilon = \omega_p/\omega_c \ll 1$) and moderately energetic ($E \ll m_e c^2$) plasma, and the index of refraction is close to 1. Based on the X-mode dispersion formula and these approximations, the simple version of the wave growth rate provided by B. Collet et al. (2023) is

$$\frac{\gamma}{\omega_c} \sim \frac{\left(\frac{\pi}{2}\epsilon_h\right)^2}{1+\left(\frac{\epsilon_c}{2\Delta\omega}\right)^2}\int_0^\pi d\theta r^2 \times \sin\theta^2 \frac{\partial}{\partial\beta_\perp} f_h(\beta_0 + r\cos\theta, r\sin\theta), \quad (2)$$

where the growth rate γ/ω_c is related to the integration of $\frac{\partial f_h}{\partial\beta_\perp}$ along a resonance circle with its center β_0 and radius r. The center $\beta_0 = k_\parallel c/\omega_c$, radius $r = (\beta_0^2 - 2\Delta\omega)^{1/2}$, frequency bandwidth $\Delta\omega = (\omega - \omega_c)/\omega_c$, normalized velocity $\beta_{\perp,\parallel} = v_{\perp,\parallel}/c$, $\epsilon_i = \frac{\omega_{pi}}{\omega_c}$ for cold ($i = c$) and hot ($i = h$) plasma,

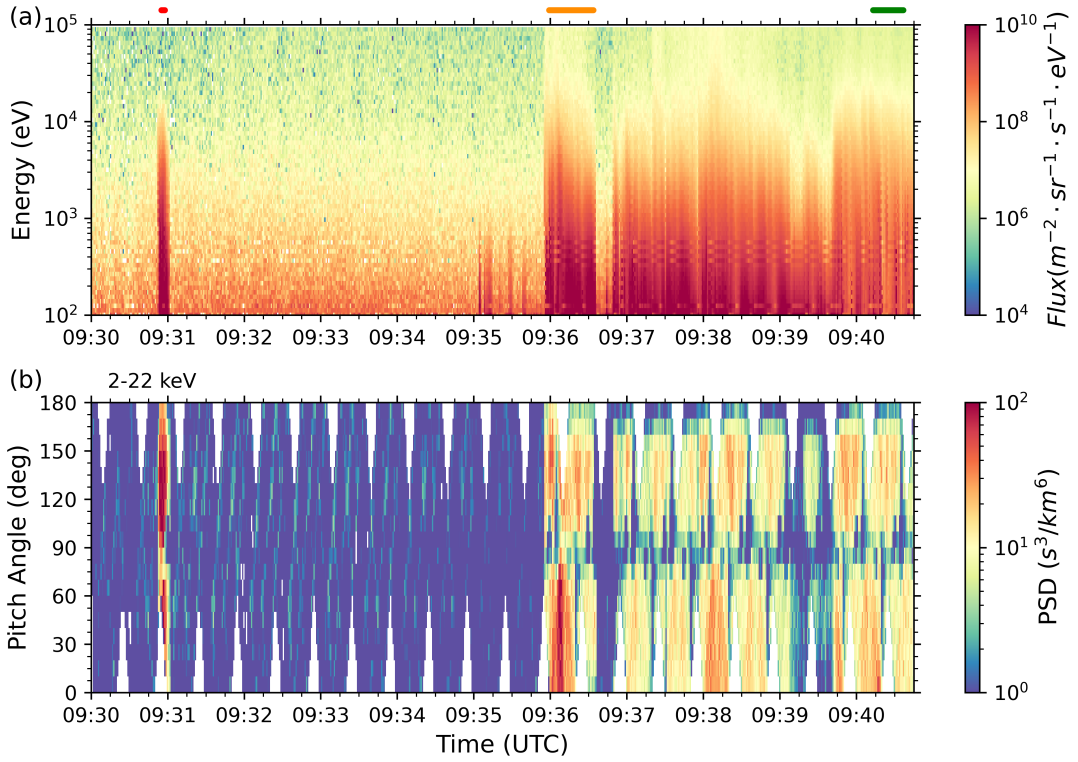

Figure 3. Juno/JADE in situ observation. (a) Electron energy flux from 100 eV to 100 keV. (b) Pitch-angle distribution of electron at 2–22 keV. The colored bars on the top mark the time intervals of the three source crossings.

and f is the normalized electron distribution $\int f d\beta^3 = 1$. The measured PSD from the JADE instrument (f in $s^3\,km^{-6}$) should be normalized by factor $c^3 10^{-24}/n_e$, where n_e is the electron density in units of cm^{-3}. Here we assume electrons with energies above 1 keV are part of the hot plasma component, used to calculate ϵ_h. This formula means the positive growth rate requires the resonance circle to pass through the positive part of the gradient $\frac{\partial f_h}{\partial \beta_\perp}$ in the distribution.

We set different resonance circles to estimate the maximum growth rate, as shown in Figures 4((d)–(f)). With the wave refraction index $N \simeq 1$, the emission angle can be estimated by $\cos(\theta_b) = \beta_0/(1 + \Delta\omega)$. Electron energy can also be obtained by center and radius, i.e., energy of the center $E_0 = 0.5 m_e \beta_0^2 c^2$ and energy of the tangent point $E_{\tan} = 0.5 m_e(\beta_0^2 - r^2)c^2$. As shown in Figure 4(d), the maximum growth rate $\gamma_{\max}/\omega_c$ of the SC1 slice is 6.4×10^{-4}, the related resonance circle (illustrated in Figure 4(a)) of the center $\beta_0 = -0.066$ and radius $r = -0.033$, and accordingly emission angle $\theta_b \approx 86.^\circ 2$, electron energy $E_0 \approx 1.1$ keV, and $E_{\tan} \approx 0.8$ keV. The frequency shift $\Delta\omega$ is 0.002 within 1.01 f_{ce}. Compared with the slice of SC1, the slices of SC2 and SC3 in panels (e) and (f) have smaller growth rates of 3.5×10^{-4} and 2.1×10^{-4}, respectively, and similar results of the resonance circle at $\theta_b \approx 86.^\circ 2$–$86.^\circ 9$, $E_0 \approx 0.7$–1.1 keV and $E_{\tan} \approx 0.6$–0.9 keV. Hereafter, we use $E_{\tan}$ for further analysis because the tangent point of the resonance circles is more likely to locate at the positive perpendicular gradient and contribute positively to the amplification of the radio wave.

Each source crossing lasted for a while. Thus, the values of the derived $E_{\tan}$ and θ_b for the maximum growth rate may vary with time, which has been summarized in Figure 4(g). The resonant energy and beam angle exhibit a correlation that remains invariant over time. This correlation originates from the equation $\cos(\theta_b) = v/c(1 + \Delta\omega)\cos(\alpha)$, where α represents the angle between the tangent line of the resonance circle and the x-axis. By fitting this equation, the estimated angle α can be derived, with the least-squares results for the three source regions (shown as the colored dashed curves) being $155.^\circ 8$, $155.^\circ 6$, and $159.^\circ 2$, respectively. It indicates that in all three source crossings, the maximum resonance circle is continuously tangent to the loss-cone boundary with a pitch angle of 155°–160° (upgoing electrons). This result suggests that the assumption made in Equation (1) for the inversion method that the maximum growth rate circle is tangent to the boundary of the loss cone is reasonable, matching this in situ case.

Beyond the resonance circle with the maximum growth rate $\gamma_{\max}/\omega_c$, regions with growth rates greater than 0.1 $\gamma_{\max}/\omega_c$ (as denoted by the contours in Figures 4(d)–(f)) are also considered as major contributors to the emission. Then, the corresponding electron energy range is 0.2–9.8 keV, and the emission angle range is $77.^\circ 0$–$88.^\circ 6$ for SC1 during 09:30:53–09:30:59. For SC2 and SC3, the energy ranges from 0.2 to 5.7 keV and the emission angle ranges from $80.^\circ 0$ to $88.^\circ 5$.

3.3. The Evolution of the Io-DAM Emission

Among the three source crossings, only the first one, the Io-related DAM, has clear imprints on the Wind and STA spectra. The inferred results of the DAM arcs in 5–15 MHz from the Wind and STA spectra are shown in Figure 5. The emission

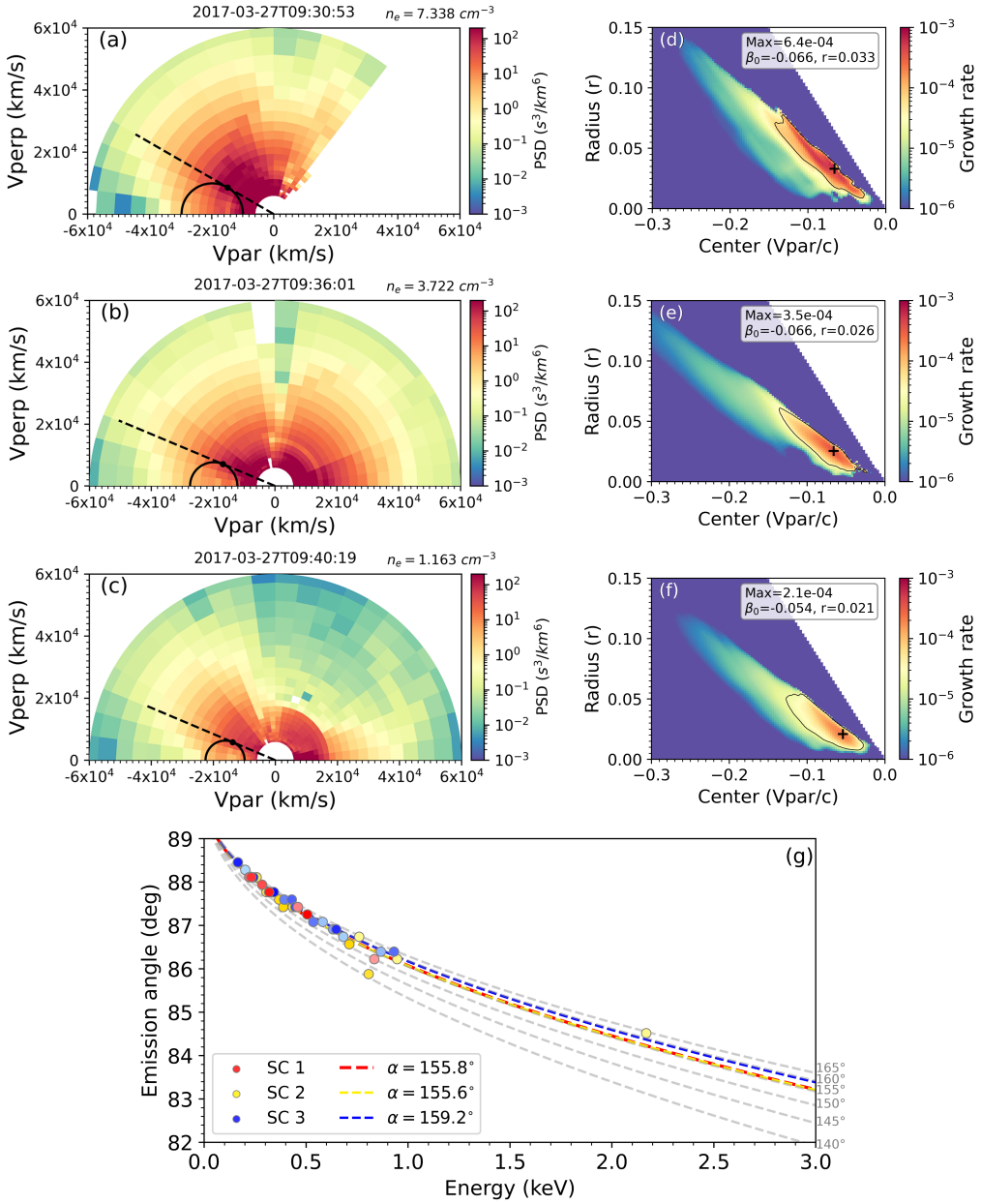

Figure 4. PSD distribution and growth rate estimation at the three source crossings. (a–c) The electron PSD distribution for SC1-SC3 at slice 09:30:53, 09:36:01, and 09:40:19, respectively. The grids consist of 25 bins in pitch angle and 32 energy channels in 100 eV to 100 keV. The part of velocity greater than 6×10^4 km s^{-1} does not have displayed data. The electron density n_e is calculated by integrating the PSD data measured by the JADE instrument. (d–f) The growth rate is distributed with a radius from 0 to 0.15 and a circle center from −0.3 to 0. The maximum growth rate is marked by black cross symbols, and the corresponding resonance circles are represented by the black semicircular curves in the left panels. The contours mean the level of 0.1 $\gamma_{\max}/\omega_c$. (g) Estimated electron energy versus emission angle during the three source crossings, where the dots are colored from light to dark with time. The fitted dashed curves for the three source crossings are given by $\cos(\theta_b) = v/c(1 + \Delta\omega)\cos(\alpha)$.

angle θ_b ranges from 70° to 87° with a mean value of 77°. The electron energy is calculated by v in Equation (1) from 0.3 to 6 keV with a mean value of 2.5 keV. The inferred active field lines are mapped to 900 km altitude above the Jovian surface, as indicated by the color-coded patch in Figure 5(c). The DAM source region is also near the Io footpath in the southern hemisphere, mainly ranging from 260° to 285° in longitude. It is roughly 7° ahead of the Io footprint, which varies from 272° to 287° during this period, marked by the yellow segmental line with two small circles at the line ends in Figure 5(c). Here the Io footpath and the Io footprints are obtained by the auroral UV spots (B. Bonfond et al. 2017). All the consistencies confirm that the first Juno source crossing and the DAM recorded by Wind and STA belong to the same event.B.

Consistently, the Juno is located at 213° in projected longitude during the first source crossings (marked by the purple asterisk in Figure 5(c)), about 6° ahead of the Io footprint, which is at 219° (purple circle in the southern hemisphere). It suggests that the Io-DAM can occur extended to a 6° shift of the Io main Alfvén wing spot (MAW), and the corresponding lead angle nearly remains unchanged for at least 2 hr as inferred from the remote-sensing observations.

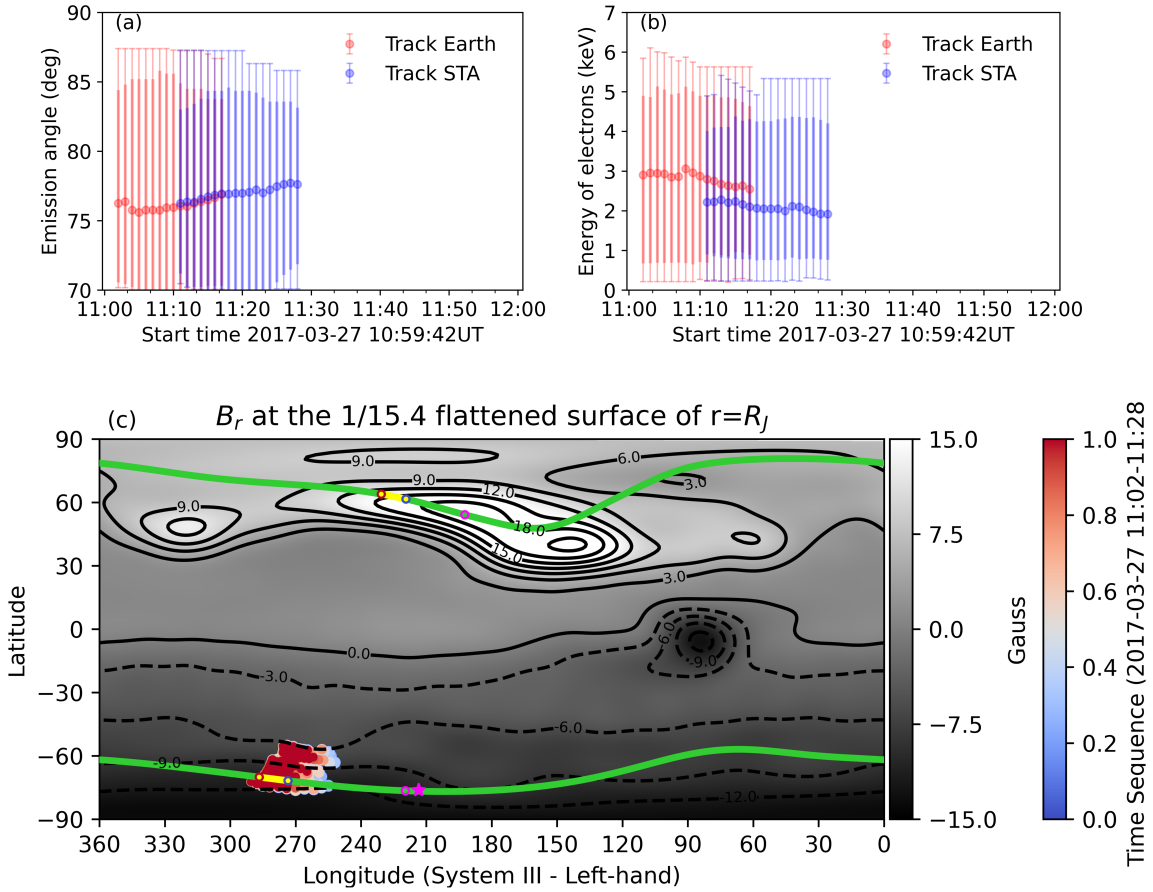

Figure 5. Inversion results based on the remote-sensing observation. (a) Emission angle and (b) active electron energy during DAM arcs observed by Wind and STA. The circles give the median values, the thin bars give the minimum and maximum values, and the thick bars give the top and bottom tenth percentiles. (c) The projected source location (blue-to-red dots) at the Jovian surface compared with Juno's projected location (purple asterisk marker) during the first source crossing. The green lines are shown as the Io footprint path, where the yellow segment is at the time of DAM arcs by remote-sensing observation and the purple hollow circle corresponds to the local observation time by Juno.

4. Conclusion and Discussion

The combination of Juno's in situ observations with remote-sensing data from Wind and STA offers a comprehensive understanding of Jupiter's decametric radio emissions. In this study, we analyzed a DAM case on 2017 March 27, of which Juno data show three source crossings, with the first one being Io-related and the other two non-Io-related. The first source crossing was observed by Wind and STA about 1.5 hr later. The combination of features in the spectra (Figure 1) allows us to identify and infer that it is the same Io-C event observed locally by Juno and remotely by both Wind and STA. The other two Juno crossings are non-Io-DAM emissions due to the large M-shell values covering 10–20. However, the non-Io-DAM emissions did not make a clear imprint on the Wind and STA spectra.

Further, we observed the peaks of electron energy flux of more than 10^4 s^3 km^{-6} in these source crossings. For 2–22 keV electrons, the loss cones with energy flux density 1 order of magnitude smaller occur consistently in the pitch angle of 150°–180°. Based on the maximum growth rate estimation, we get the resonance circles of the three source crossings. For the first Io-related source crossing, the maximum growth rate is 6.4×10^{-4}, the overall energy range is 0.2–9.8 keV, and the emission angle is 77.°0–88.°6. For the second and the third source crossing for non-Io-DAM events, the maximum growth rate is about 3×10^{-4}, the emission angle is 80.°0–88.°5, and the electron energy ranges from 0.2 to 5.7 keV.

Moreover, the emission parameters (e.g., emission angle, resonant electron energy, and source location) of the Io-DAM are inferred based on Wind and STA remote-sensing observation. Compared with the in situ result for the Io-DAM event, the inferred emission angle covers the range of estimated in situ results but with a smaller overall mean value (ranges from 70° to 87° with a mean value of 77°). The electron energy is from 0.3 to 6 keV, similar to the in situ result, but with a lower maximum.

The study of this Io-DAM event suggests the existence of a source region lasting at least 1.5 hr with the Io flux tube corotation, observed by in situ and remote sensing, respectively. The Io-DAM source location has a 6° shift of the MAW, and the corresponding lead angle nearly remains unchanged for at least 1.5 hr, as inferred from the remote-sensing observations. The inferred results are consistent with the in situ results, indicating that the remote-sensing inversion method is reliable and suitable for the DAM emissions dominated by loss-cone distributions.

As noted by B. Collet et al. (2023), shell-type distributions can also contribute to CMI generation. In theory, emission driven by a shell-type distribution should occur at frequencies

slightly lower than the local cyclotron frequency. However, as shown in Figure 1, no significant emission in the spectra is detected at frequencies below the local cyclotron frequency in this event. Moreover, the electron distribution is more consistent with a loss-cone type rather than a shell type, as shown in Figures 3 and 4. Therefore, in this study, we adopt the loss-cone distribution as the basis for constructing the inversion method. To better capture these other potential electron distributions, future work could focus on optimizing the remote-sensing inversion method to account for shell-type or other non-loss-cone distributions. This would require further joint observational studies aimed at understanding radiation from a broader range of electron distribution types.

In addition, although 59 source crossings were observed in situ, only one event was detectable by both STA and Wind remotely. The visibility of these emissions in remote sensing may be influenced by several factors, including emission intensity, duration, source region distribution, and the geometrical relationship between the emission cone and the remote observers. Understanding these factors more comprehensively will be essential for improving the accuracy and reliability of remote sensing in future DAM studies.

Acknowledgments

We acknowledge the use of the data from Juno (Waves, MAG, JADE instruments) and the radio instruments on board the Wind and STEREO-A spacecraft. We thank the Planetary Data Reader (pdr) team for providing the code to read the Juno data (S. V. Brown et al. 2024). We also thank Robert Wilson and Minyi Long for advice on data processing. The work is supported by the NSFC (42188101, 42374197) and the Innovation Program for Quantum Science and Technology (2021ZD0300302). Y.W. is particularly grateful for the support of the New Cornerstone Science Foundation through the Xplorer Prize.

Facilities: Wind (WAVES), STEREO (WAVES).

Author Contributions

Conceptualization: Y.W., R.Z.; data analysis: R.Z., Y.W., C. W.; software: R.Z., Y.W.; writing—review and editing: all authors.

Appendix
Valuation of Interpolation Methods for Electron Distribution Data

When calculating the maximum growth rate, the integrated results may be inaccurate due to the resolution of the PSD data (energy in 32 bins from 100 eV to 100 keV and look direction in bins of $7.^{\circ}5$) measured by Juno/JADE. Thus, we test some different interpolations in the 2D grid to get more accurate calculations by setting a loss-cone–beam distribution, as shown in Figure 6.

The initial distribution in panel (a) is high resolution for comparison, and the sample in panel (b) is low resolution as in the PSD data. Panels (c) and (d) show the linear and cubic interpolated data based on the sample data. Then, we calculate the perpendicular gradient along the line and the circle for these four distributions. The result in panels (e) and (f) show that the cubic interpolation has the more accurate result in a perpendicular gradient along the line and the circle matching the initial result. In this paper, the data have been cubic interpolated for growth rate calculation. In addition, this test suggests that the sample result cannot be used directly due to the large deviation from the initial result.

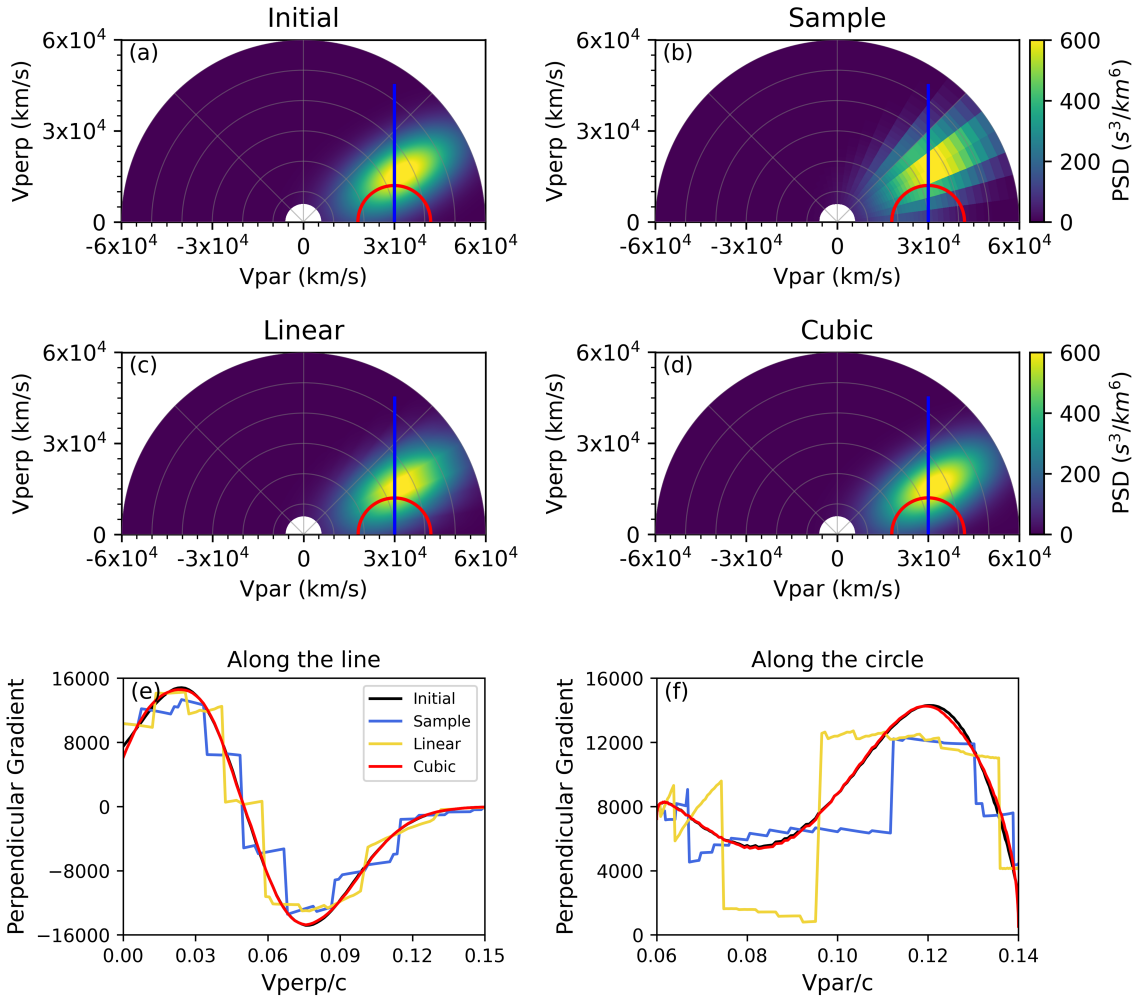

Figure 6. Test for calculation perpendicular gradient based on different processed data: (a) initial beam distribution with high resolution, (b) sample data with low resolution as in the directly measured data in the main text, (c) linear interpolation, and (d) cubic interpolation based on the sample data. Panels (e) and (f) show the perpendicular gradient calculated along the blue line and red circle in the four distributions.

ORCID iDs

Ruobing Zheng https://orcid.org/0009-0000-8229-9605
Yuming Wang https://orcid.org/0000-0002-8887-3919
Chuanbing Wang https://orcid.org/0000-0001-6252-5580

References

Bagenal, F., Adriani, A., Allegrini, F., et al. 2017, SSRv, 213, 219
Bonfond, B., Grodent, D., Gérard, J.-C., et al. 2009, JGRA, 114, A07224
Bonfond, B., Saur, J., Grodent, D., et al. 2017, JGRA, 122, 7985
Bougeret, J. L., Goetz, K., Kaiser, M. L., et al. 2008, SSRv, 136, 487
Bougeret, J. L., Kaiser, M. L., Kellogg, P. J., et al. 1995, SSRv, 71, 231
Brown, S. V., St. Clair, M., Million, C., et al. 2024, JOSS, 9, 7256
Collet, B., Lamy, L., Louis, C. K., et al. 2023, in Planetary, Solar and Heliospheric Radio Emissions IX, ed. C. K. Louis et al. (Dublin Institute for Advanced Studies), 212
Connerney, J. E. P., Benn, M., Bjarno, J. B., et al. 2017, SSRv, 213, 39
Connerney, J. E. P., Timmins, S., Herceg, M., & Joergensen, J. L. 2020, JGRA, 125, e2020JA028138
Connerney, J. E. P., Timmins, S., Oliversen, R. J., et al. 2022, JGRE, 127, e2021JE007055
Gurnett, D. A., Kurth, W. S., Kirchner, D. L., et al. 2004, SSRv, 114, 395
Hess, S., Cecconi, B., & Zarka, P. 2008, GeoRL, 35, L13107
Hess, S., Pétin, A., Zarka, P., Bonfond, B., & Cecconi, B. 2010, P&SS, 58, 1188
Konovalenko, A., Sodin, L., Zakharenko, V., et al. 2016, ExA, 42, 11
Kurth, W. S., Hospodarsky, G. B., Kirchner, D. L., et al. 2017, SSRv, 213, 347
Lamy, L., Colomban, L., Zarka, P., et al. 2022, JGRA, 127, e2021JA030160
Le Quéau, D., Pellat, R., & Roux, A. 1984a, JGRA, 89, 2831
Le Quéau, D., Pellat, R., & Roux, A. 1984b, PhFl, 27, 247
Lecacheux, A. 2000, GMS, 119, 321
Louarn, P., Allegrini, F., McComas, D. J., et al. 2017, GeoRL, 44, 4439
Louarn, P., Allegrini, F., McComas, D. J., et al. 2018, GeoRL, 45, 9408
Louis, C. K., Hess, S. L. G., Cecconi, B., et al. 2019a, A&A, 627, A30
Louis, C. K., Louarn, P., Allegrini, F., Kurth, W. S., & Szalay, J. R. 2020, GeoRL, 47, e2020GL090021
Louis, C. K., Prangé, R., Lamy, L., et al. 2019b, GeoRL, 46, 11606
Marques, M. S., Zarka, P., Echer, E., et al. 2017, A&A, 604, A17
McComas, D. J., Alexander, N., Allegrini, F., et al. 2017, SSRv, 213, 547
Pritchett, P. L. 1986, PhFl, 29, 2919
Szalay, J. R., Allegrini, F., Bagenal, F., et al. 2020, GeoRL, 47, e2019GL086527
Wang, Y., Jia, X., Wang, C., et al. 2020, E&PP, 4, 1
Wang, Y., Zheng, R., Jia, X., et al. 2022, E&PP, 6, 13
Wu, C. S. 1985, SSRv, 41, 215
Wu, C. S., & Lee, L. C. 1979, ApJ, 230, 621
Zarka, P., Tagger, M., Denis, L., Girard, J. N., Konovalenko, A., Atemkeng, M., et al. 2015, in 2015 International Conference on Antenna Theory and Techniques (ICATT) (IEEE)
Zheng, R., Wang, Y., Li, X., Wang, C., & Jia, X. 2023, A&A, 673, A106